## ARTICLE

# YAP and TAZ regulate cell volume

Nicolas A. Perez-Gonzalez[1]\*, Nash D. Rochman[1]\*, Kai Yao[2]\*, Jiaxiang Tao[2], Minh-Tam Tran Le[1], Shannon Flanary[1], Lucia Sablich[1], Ben Toler[1], Eliana Crentsil[1], Felipe Takaesu[1], Bram Lambrus[3], Jessie Huang[4], Vivian Fu[6], Pragati Chengappa[5]iD, Tia M. Jones[5], Andrew J. Holland[3]iD, Steven An[4]iD, Denis Wirtz[1,7]iD, Ryan J. Petrie[5]iD, Kun-Liang Guan[6], and Sean X. Sun[1,2,7]iD

How mammalian cells regulate their physical size is currently poorly understood, in part due to the difficulty in accurately quantifying cell volume in a high-throughput manner. Here, using the fluorescence exclusion method, we demonstrate that the mechanosensitive transcriptional regulators YAP (Yes-associated protein) and TAZ (transcriptional coactivator with PDZ-binding motif) are regulators of single-cell volume. The role of YAP/TAZ in volume regulation must go beyond its influence on total cell cycle duration or cell shape to explain the observed changes in volume. Moreover, for our experimental conditions, volume regulation by YAP/TAZ is independent of mTOR. Instead, we find that YAP/TAZ directly impacts the cell division volume, and YAP is involved in regulating intracellular cytoplasmic pressure. Based on the idea that YAP/TAZ is a mechanosensor, we find that inhibiting myosin assembly and cell tension slows cell cycle progression from G1 to S. These results suggest that YAP/TAZ may be modulating cell volume in combination with cytoskeletal tension during cell cycle progression.

## Introduction

The question of cell size is at the core of how organisms coordinate cell growth and proliferation. Cell volume dysregulation has been broadly used as a biophysical marker for disease, notably cancer (Kozma and Thomas, 2002; Dannhauser et al., 2017). At a basic level, with increasing cell size, the cell surface–to-volume ratio shrinks, potentially altering the ratio of membrane-bound components to cytoplasmic components, thus fundamentally changing both inter- and intracellular dynamics. Recently, substantial progress has been made toward understanding cell volume regulation, largely enabled by the development of quantitative tools to directly monitor cell cycle progression (Sakaue-Sawano et al., 2008), cell dry mass (Mir et al., 2011; Sung et al., 2013), buoyant cell mass (Son et al., 2012), cell total protein content (Kafri et al., 2013; Ginzberg et al., 2018), and single-cell volume in normal culture (Guo et al., 2017; Varsano et al., 2017; Cadart et al., 2018; Wang et al., 2018). Here, to study cell volume in a high-throughput manner, we use the fluorescence exclusion (FX) method developed by Bottier and others (Bottier et al., 2011; Cadart et al., 2017; Perez-Gonzalez et al., 2018). Using this robust and accurate method, it was revealed that mitotic cells swell suddenly before cytokinesis (Zlotek-Zlotkiewicz et al., 2015) and that some types of cells show an adder-like behavior to achieve cell volume homeostasis (Cadart et al., 2018).

In previous work, we demonstrated a relationship between cell volume, cell cortical tension (measured by phosphorylated myosin light chain [pMLC]), and Yes-associated protein/transcriptional coactivator with PDZ-binding motif (YAP/TAZ) activity (measured by nuclear portion of YAP/YAZ; Perez-Gonzalez et al., 2018; Wang et al., 2018). YAP/TAZ has been previously reported as a key regulator in organ size control (Zhao et al., 2007, 2008; Tumaneng et al., 2012) and in mechanotransduction (Dupont et al., 2011; Piccolo et al., 2014; Chang et al., 2018). We reported that the mean YAP/TAZ activity is a good predictor of mean cell volume across different cell lines and substrates of varying stiffness. Here, we demonstrate using single-cell volume measurements that YAP/TAZ plays an important role in cell volume regulation. The relationship between the Hippo pathway and cell morphology has already been hinted at in the literature, largely relying on flow cytometry and visual inspection (Horie et al., 2016; Plouffe et al., 2016). In this work, we measure cell volume of human embryonic kidney (HEK) cells across a group of Hippo pathway CRISPR knockout (KO) cell lines with varying degrees of YAP/TAZ activity and demonstrate that the cell volume is positively correlated with YAP/TAZ activity. Moreover, the role of YAP/TAZ in cell volume regulation must not be limited to its influence on the total cell cycle time or cell shape, nor through its connection with the mechanistic

......................................................................................................................................................................
[1]Department of Chemical and Biomolecular Engineering, Johns Hopkins University, Baltimore, MD; [2]Department of Mechanical Engineering, Johns Hopkins University, Baltimore, MD; [3]Department of Molecular Biology and Genetics, Johns Hopkins University, School of Medicine, Baltimore, MD; [4]Department of Environmental Health and Engineering, Johns Hopkins Bloomberg School of Public Health, Baltimore, MD; [5]Department of Biology, Drexel University, Philadelphia, PA; [6]Department of Pharmacology and Moores Cancer Center, University of California, San Diego, La Jolla, CA; [7]Physical Sciences in Oncology Center, Johns Hopkins University, Baltimore, MD.

\*N.A. Perez-Gonzalez, N.D. Rochman, and K. Yao contributed equally to this paper;   Correspondence to Sean X. Sun: ssun@jhu.edu.

target of rapamycin (mTOR) pathway. We show that YAP/TAZ directly impacts cell division volume. Since YAP/TAZ is a central player in mechanotransduction (Dupont et al., 2011; Piccolo et al., 2014; Chang et al., 2018), we found that YAP/TAZ activity is directly correlated with cell cytoskeletal tension, and modulating cell tension can delay cell cycle progression. These results suggest that cell tension and the Hippo pathway work together to control the G1/S cell cycle checkpoint, thus determining the cell volume.

## Results

We used the FX method to quantify single-cell volume as previously described (Perez-Gonzalez et al., 2018). Briefly, we fabricated microchannels coated with collagen I (Fig. 1 A). Single cells were seeded at low density and allowed to adhere. After cell adhesion, medium was infused with fluorescent FITC-Dextran, which evenly labeled the cell surroundings but remained exclusively in the extracellular medium, exhibiting minimal endocytosis within 5 h (Fig. 1 B). The epifluorescent images obtained were then segmented (Fig. 1 C), and the 3D cell volume was computed as depicted in Fig. 1 D and reconstructed (Fig. S1, A–C).

### YAP/TAZ regulate single cell volume

Previous work reported positive correlations between the 2D cell adhesion area with cell YAP/TAZ expression (Plouffe et al., 2018) and the 3D cell volume with cell YAP/TAZ activity (defined as nuclear YAP/TAZ content; Perez-Gonzalez et al., 2018). We sought to further elucidate the relationship between the Hippo pathway and cell volume through the utilization of CRISPR KOs for Hippo genes (Fig. 1 E). Other studies have shown that activation of the Hippo pathway is followed by the phosphorylation of YAP/TAZ, leading to cytoplasmic localization and inhibition of YAP/TAZ (Zhao et al., 2007; Fig. 1 E). In this pathway, LATS1/2 is responsible for YAP/TAZ phosphorylation and inactivation; therefore, their absence increases YAP/TAZ nuclear localization and subsequent activity. Characterization and validations of these CRISPR KOs were performed previously (Plouffe et al., 2016). We further validated these cells in this work using quantitative immunofluorescence (qIF; Fig. 1 F) and Western blotting (Fig. 1 G). More details on qIF can be found in Materials and methods (Fig. S1, D–F). We found that average nuclear YAP/TAZ activity is increased in the LATS1/2 double knockout (dKO) cells compared with the parental HEK 293A, although there is some overlap between the populations. Similarly, the TAZ KO and YAP KO cells exhibit a significant decrease in nuclear YAP/TAZ. Finally, qIF for the YAP/TAZ dKO showed low YAP/TAZ activity and low variability, suggesting that this corresponds to nonspecific binding and is an indication of the level of background noise in our measurement.

Across the four CRISPR-generated cell lines and the parental HEK 293A, we found that the average amount of nuclear YAP/TAZ strongly correlated with the average cell volume (Fig. 1, H and I), as seen before for cells growing on substrates of varying stiffness (Perez-Gonzalez et al., 2018). These cell volume results are further confirmed by shRNA of YAP and TAZ in the same cells (Fig. S1), although shRNA only partially reduced nuclear

YAP/TAZ levels. Accordingly, when comparing volume distributions of all five cell lines (Fig. 1 H), we found that YAP/TAZ activity correlates with an increasing abundance of larger cells, e.g., LATS1/2 dKO has mostly larger cells, while YAP/TAZ dKO has mostly smaller cells. When comparing the average cell volume between populations, we observed an increase of 3.01% in the LATS1/2 dKO. As YAP/TAZ expression decreased, we observed a volume decrease of 15.8% in the TAZ KO, 18.2% in the YAP KO, and 27.2% in the YAP/TAZ dKO (Fig. 1 I). It is worth noting that under favorable culture conditions, LATS1/2 are largely inhibited and YAP/TAZ are active. This may explain why LATS1/2 dKO produced only a modest effect on cell size, whereas YAP/TAZ KO produced more dramatic effects. Additionally, we assessed the cell spreading area, noticing that volume and area are positively correlated with each other, but in some cases, a volume change could be observed in the absence of an area change (Fig. S1, G and H). We also used two more common approaches to assess cell size: Coulter Counter (Fig. 1 K; Conlon et al., 2001; Burke et al., 2012) and flow cytometry (Fig. 1 J; Plouffe et al., 2018). Despite requiring the cells to be resuspended, grossly changing their morphology, both the Coulter Counter measurements (Fig. 1 J) and flow cytometry measurements showed a similar cell volume trend (Fig. 1 K).

In addition to the static cell volume, we examined how the cell volumetric growth rate as well as the volume at the beginning and end of the cell cycle vary with the presence of YAP/TAZ. We tracked single-cell volume for 5 h within the fabricated microchannels described above (Fig. 1 L) and obtained cell growth trajectories (Fig. 1 M) for each of the five cell lines. A dye endocytosis assay was also performed to rule out possible differences in endocytic rates among the five cell lines (Fig. S2 C). A portion of cells undergoing mitosis were observed, for which we measured the volume immediately before and after division (hereafter referred to as division and birth volumes). We found that both the cell birth volume and the division volume increased with increased activity of YAP/TAZ (Fig. 1 N), explicitly confirming that the observed volumetric change corresponds to an intrinsic change in volume within the population.

### Single-cell growth rate is proportional to cell size and follows a universal growth law

To further understand single-cell growth, we quantified added volume per unit time (volumetric growth rate) for many single cells. Fig. 2 A shows the average cell growth trajectory in blue and the standard deviation as the gray area for each of the five cell lines. Fig. 2 A also displays sample trajectories for each of the cell lines as an inset on the top right of each figure. The degree to which these cell lines display obvious mitotic swelling, as previously reported in the literature (Zlotek-Zlotkiewicz et al., 2015), varies with YAP/TAZ activity. The TAZ KO, parental cell line, and LATS1/2 dKO display a sharp volume increase and decrease right before division. However, the YAP KO and YAP/TAZ dKO show reduced or unresolvable mitotic swelling at the time resolution used in this study, suggesting that YAP may play a role in mitotic swelling. To quantify growth trajectories and obtain the growth rate, we fitted an exponential growth law to each trajectory, obtaining $dV/dt$ versus $V$ for each cell (Fig. 2, B

Perez-Gonzalez et al.
YAP and TAZ regulate cell volume

**Journal of Cell Biology** 3473
https://doi.org/10.1083/jcb.201902067
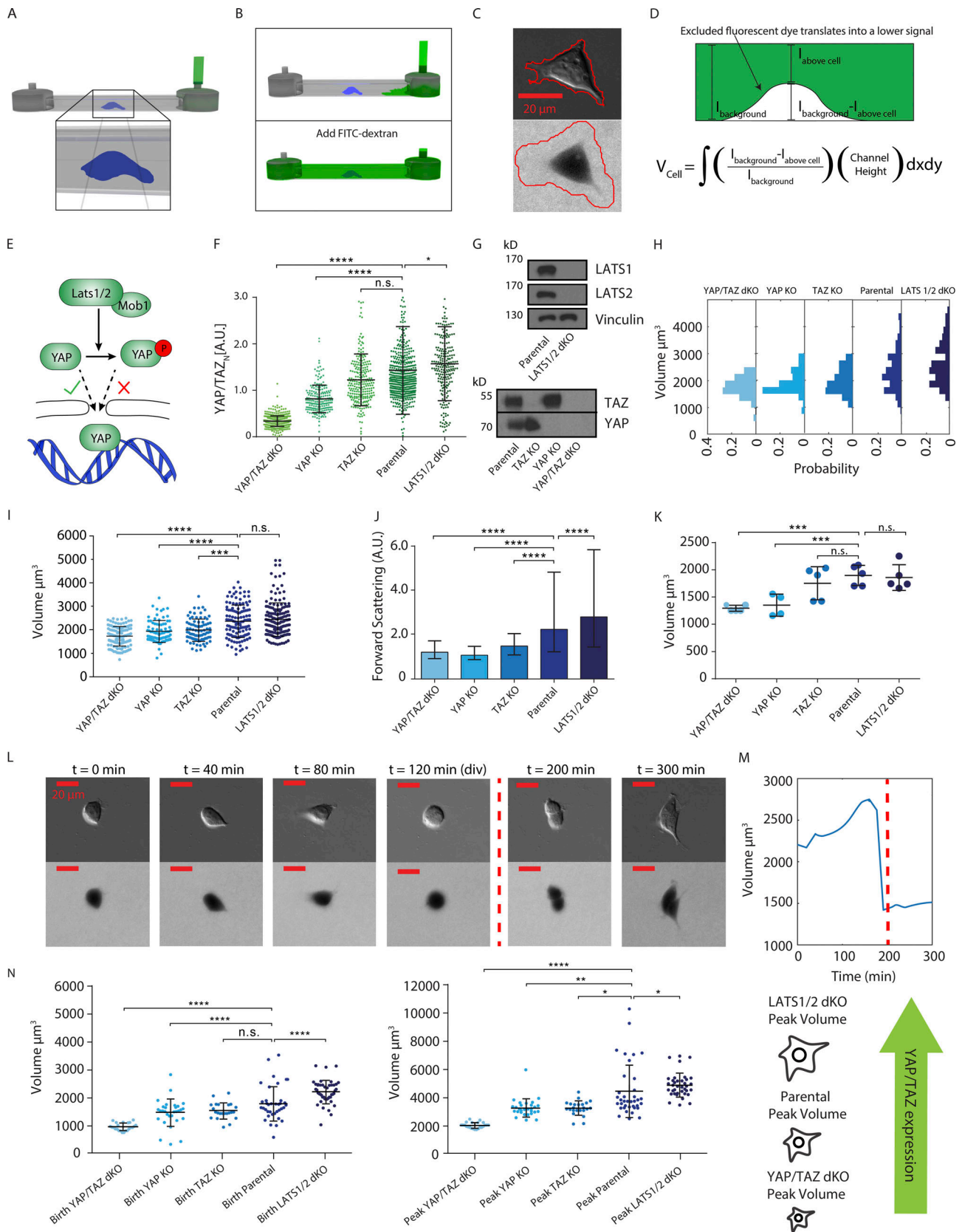
Figure 1. **YAP and TAZ proteins are regulators of single-cell cell volume. (A–D)** Cartoons depicting the FX method. **(A)** Side view of microdevice. **(B)** Cells are seeded in the device before adding the fluorescent dye (top). The dye is not membrane permeable and therefore is excluded from the cell interior (bottom). **(C)** Sample DIC and fluorescent images for volume calculation. **(D)** Conversion of fluorescent image into volume. **(E)** Hippo pathway cartoon, showing key elements of the pathway. **(F)** Nuclear YAP/TAZ content by qIF. Hippo pathway activity was assessed by qIF in the parental line and all CRISPR KOs (N$_{YAPTAZ\ dKO}$ = 223,

$N_{YAP\ KO}$ = 156, $N_{TAZ\ KO}$ = 287, $N_{HEK\ 293A}$ = 331, $N_{LATS1/2\ dKO}$ = 207). **(G)** Hippo pathway KO validation. Western blots were performed to assess YAP and TAZ expression in all CRISPR KOs. **(H)** Volume measurements of Hippo pathway KOs via the FX method. Panel shows the distribution for each cell line ($N_{YAPTAZ\ dKO}$ = 130, $N_{YAP\ KO}$ = 118, $N_{TAZ\ KO}$ = 162, $N_{HEK\ 293A}$ = 135, $N_{LATS1/2\ dKO}$ = 185). **(I)** Volume measurements of Hippo pathway KOs via the FX method. Single-cell volume distributions are shown as scatter plots. ($N_{YAPTAZ\ dKO}$ = 130, $N_{YAP\ KO}$ = 118, $N_{TAZ\ KO}$ = 162, $N_{HEK\ 293A}$ = 135, $N_{LATS1/2\ dKO}$ = 185). **(J)** Volume measurement of Hippo pathway KOs via flow cytometry. Number of experiments: three biological repeats for each cell line with ~15,000 cells per repeat. **(K)** Volume measurement of Hippo pathway KOs via Coulter Counter ($N_{YAPTAZ\ dKO}$ = 5, $N_{YAP\ KO}$ = 4, $N_{TAZ\ KO}$ = 5, $N_{HEK\ 293A}$ = 5, $N_{LATS1/2\ dKO}$ = 5). **(L)** Cell volume as a function of time. Cell volume was monitored over time for 5 h. **(M)** Volume trajectory. Sample cell growth trajectory is shown as a function of time for a single cell. **(N)** Daughter cell volume and volume before division. Averages are presented for the parental cell line and all Hippo pathway KOs. Error bars represent standard deviation of the data. n.s., P ≥ 0.05; *, P < 0.05; **, P < 0.01; ***, P < 0.005; ****, P < 0.001.

and C). Additionally, we fitted linear growth curves to the same data (Fig. S2, A and B) since it has been noted that it is difficult to distinguish an exponential growth law from a linear growth law (Ginzberg et al., 2015), largely due to the small range of volumes observed within a single cell cycle (roughly a twofold variation). Indeed, in the next section, we discuss that the growth law is unlikely to have a measurable influence on the average cell volume; however, our results show that the volumetric growth rate is proportional to the cell volume across populations. When all growth trajectories for all cells are overlaid (Fig. 2 D), it is apparent that all five cell lines follow a similar growth law, i.e., the growth rate $dV/dt \propto V$ regardless of YAP/TAZ activity (and regardless of whether $dV/dt$ for each cell was fitted assuming an exponential or linear dependence on $V$). The combination of multiple cell lines spanning a much larger range of volumes lends greater confidence to the observation that across populations there is a strong linear dependence of $dV/dt$ on $V$, indicating an exponential volumetric growth rate with respect to cell volume.

The data show that the presence of YAP/TAZ seems to be regulating $dV/dt$, with increasing YAP/TAZ activity associated with slightly higher $dV/dt$. At first glance, this might seem to be the critical observation needed to explain how YAP/TAZ and Hippo are regulating cell volume. Thus, it is natural to focus on the regulation of $dV/dt$. However, average cell volume does not depend on growth rate alone, but also on the duration of the cell cycle, $\tau$. It can be shown theoretically that the average cell volume is slightly less than $(3/2\tau)dV/dt$ (see Materials and methods for details), where $\tau$ is the average cell cycle duration. YAP/TAZ has also been shown to regulate the duration of the cell cycle (Plouffe et al., 2018; Fig. 3 A), with increasing YAP/TAZ activity associated with smaller $\tau$. It is clear that YAP/TAZ is affecting $dV/dt$ and $\tau$ in opposite ways (and examining the trend in $\tau$ alone is also insufficient to explain volume regulation; see the next section). A larger increase is observed for $dV/dt$ than what would be necessary to compensate for the observed decrease in $\tau$ and keep the average volume constant. How YAP/TAZ skews this balance in favor of increased $dV/dt$ remains unclear, and more information regarding the role of YAP/TAZ in cell cycle regulation may be needed to understand this phenomenon (see Fig. 5 for more discussion).

Due to endocytosis of FITC-Dextran on longer time scales (>8 h), we are not able to obtain growth trajectories for the complete cell cycle. Therefore, we are unable to observe correlations between the birth volume and the added volume at the single-cell level; however, we do observe a population of cells that exhibit near-zero growth over 5 h, which we interpret as quiescent cells. We observed that cells in quiescence can also transition out of quiescence and grow again. Finally, it is worth noting that growing cells show

a continuous and proportional growth-rate-versus-volume curve, with no visible dependence on cell cycle phase.

## Volume differences across Hippo pathway KOs are not explained by cell cycle duration or volumetric growth law

It is clear how changing the birth and division volumes may affect the average population volume; however, it is also possible that the cell cycle duration, cell cycle phase distribution, and growth rate as a function of volume could impact the mean volume while keeping the birth and division volumes constant. For example, suppose we have a hypothetical cell for which $dV/dt$ is positive during G1 and zero during S and G2. Further suppose that we can lengthen the duration of G2 while keeping the birth and division volumes constant. For that cell, lengthening G2 will increase the average volume of the population, since each cell will spend more time at its maximum volume. We did not observe growth laws of this type in the cell lines used for this article; however, we sought to examine how small variations in the growth law (e.g., comparing the exponential and linear models) may affect average volume. In previous work (Rochman et al., 2018), we discussed how some conserved quantities may be used to calculate population averages of age-dependent measurements. In particular, volume and DNA distributions for an ensemble may be calculated given the growth trajectory, $V(t)$, and DNA content progression, $DNA(t)$ (see Materials and methods for details). We may compare two cell volume distributions: one obtained with a long cell cycle duration (Fig. 3 B, red curve) and one obtained with a short duration (Fig. 3 B, black curves). The $V(t)$ curve for the ensemble with the shorter duration will have a steeper rise regardless of whether the growth law is linear or exponential (Fig. 3 C); however, the resultant volume distributions will be negligibly different (and the difference depends only on whether the growth rate is linear or exponential, not on the cell cycle duration) on the scale of variation we observe across the CRISPR KOs (Fig. 3 D; see Materials and methods for details). When the ratio of time spent in each cell cycle phase G1, S, and G2 is conserved, as observed across the CRISPR KOs (Fig. 3 F), we also predict the DNA distribution to be independent of cell cycle duration (Fig. 3 E). Thus, cell cycle duration is not predicted to impact the volume distribution, and while modifying the growth law may modestly change the mean cell cycle duration, only extremely nonlinear trends could replicate the magnitude of variation we observe across the CRISPR KOs. Therefore, any impact the Hippo pathway and YAP/TAZ activity may have on the volumetric growth law or cell cycle duration (Fig. 3 A) alone is unable to explain the volume variation across the CRISPR KOs.
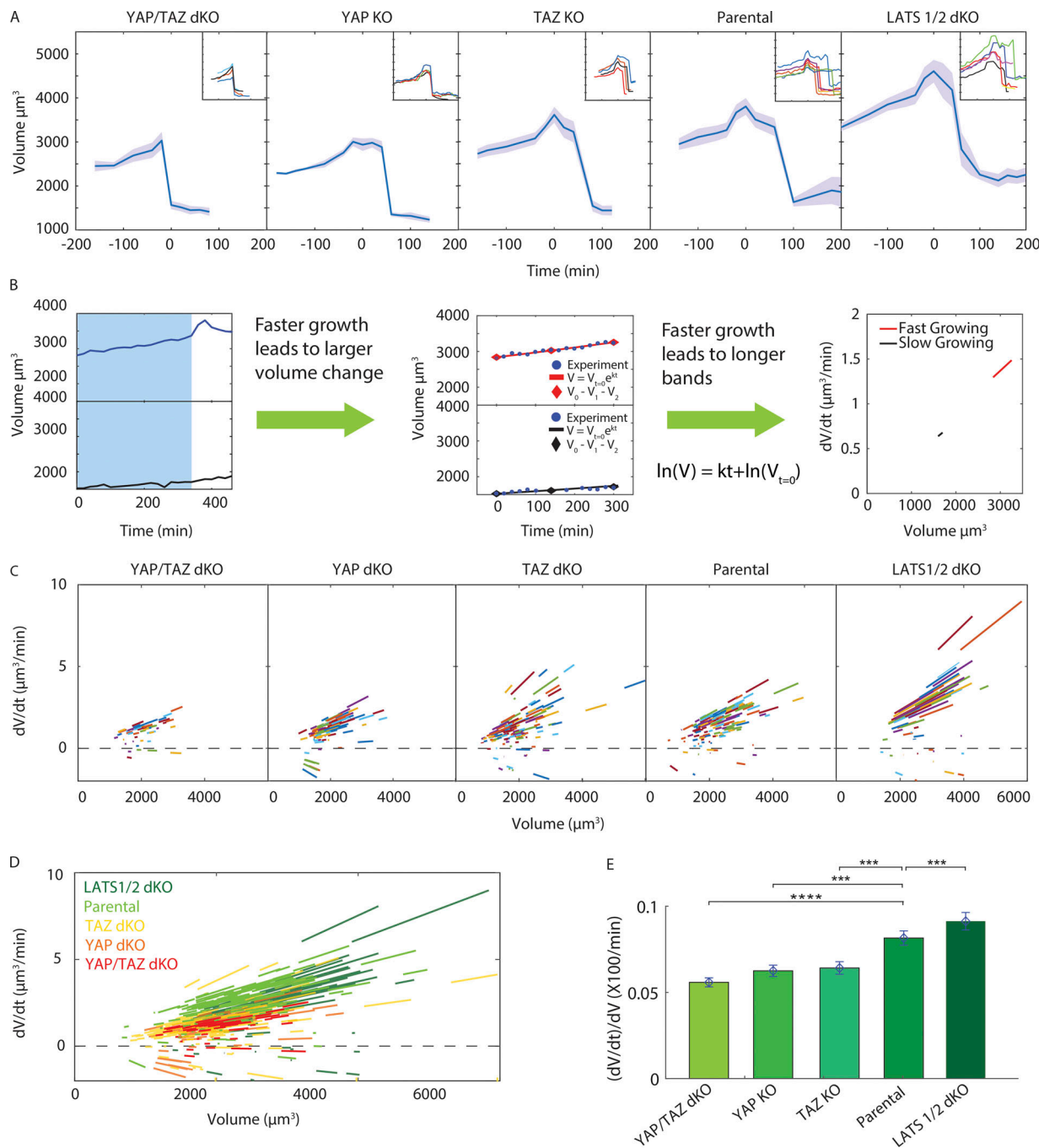
**Figure 2. Growth rate quantification of Hippo pathway KOs. (A)** Average cell growth trajectory. The average trajectory is shown in blue, and the first standard devition is shown by the gray area. Sample cell growth trajectories are displayed in an inset to qualitatively show their behavior. **(B)** Extraction of growth rate, $dV/dt$, as a function of time. Left panel shows the sample trajectories of two cells, a small cell (bottom panel) and a big cell (top panel). For each cell, we use three points to determine the constant for exponential growth (middle panel). Sample plot of single-cell growth rate versus the volume of that cell (right panel). **(C)** Growth rate versus cell at single-cell level ($N_{YAPTAZ\ dKO} = 130$, $N_{YAP\ KO} = 118$, $N_{TAZ\ KO} = 162$, $N_{HEK\ 293A} = 175$, $N_{LATS1/2\ dKO} = 185$). **(D)** Growth rate curves overlapped for all Hippo KOs. With increasing YAP/TAZ activity, the growth rate is slightly higher for the same cell volume. **(E)** The average slope of $dV/dt$ versus $V$ ($N_{YAPTAZ\ dKO} = 130$, $N_{YAP\ KO} = 118$, $N_{TAZ\ KO} = 162$, $N_{HEK\ 293A} = 175$, $N_{LATS1/2\ dKO} = 185$). Error bars represent standard deviation of the data. ***, $P < 0.005$; ****, $P < 0.001$.

## Volume variations are not explained by cell geometry

In a previous article (Perez-Gonzalez et al., 2018), we showed that cell geometry plays a major role in cortical force balance and is an important factor in determining cell size. In principle, regulating the spatial distribution of cortical contractility while conserving the osmotic gradient across the cell cortex could result in large changes in cell volume. For example, suppose increasing YAP/TAZ activity decreases cell protrusivity, resulting in a more hemispherical cell shape and thus higher curvature. This higher curvature, with the same pMLC
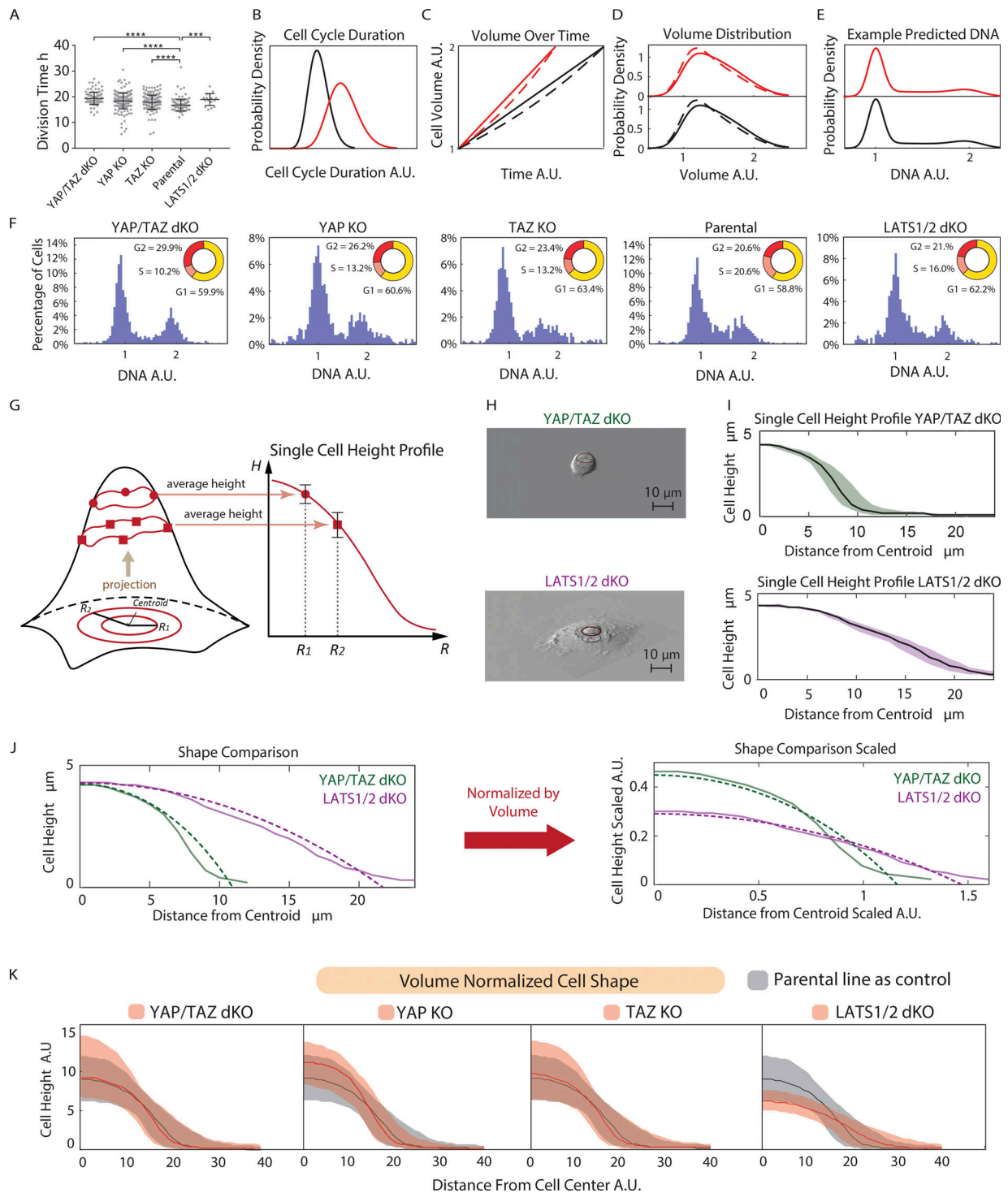
Figure 3. **Volume differences across Hippo pathway KOs are independent of cell growth dynamics and cell geometry. (A)** YAP/TAZ decreases cell cycle duration and doubling time. Cell cycle duration and bulk doubling time for the HEK 293A and five KO lines ($N_{YAPTAZ\ dKO}$ = 107, $N_{YAP\ KO}$ = 216, $N_{TAZ\ KO}$ = 186, $N_{HEK\ 293A}$ = 122, $N_{LATS1/2\ dKO}$ = 18). Error bars represent standard deviation of the data. **(B)** Two populations with different cell cycle duration are considered using a mathematical model (Materials and methods). Long cell cycle duration and short cell cycle duration. **(C)** Two growth schemes are considered, linear or exponential growth. A solid red line represents linear growth with short cell cycle duration, and a dashed red line represents exponential growth with short cell cycle duration. The solid black line represents linear growth with long cell cycle, and a dashed black line represents exponential growth with long cell cycle duration. **(D)** Volume distributions for each case. **(E)** Computed DNA distribution. Predicted from the mathematical model in Materials and methods. **(F)** YAP/TAZ does not change the cell cycle phase distribution. A comparison of the DNA distributions from Hoechst staining across the cell lines showed no significant difference (inset, cell cycle fraction; $N_{YAPTAZ\ dKO}$ = 1137, $N_{YAP\ KO}$ = 961, $N_{TAZ\ KO}$ = 774, $N_{HEK\ 293A}$ = 1202, $N_{LATS1/2\ dKO}$ = 876). **(G)** The role of YAP/TAZ in 3D cell shape: cartoon of analysis. Cartoon depicts single-cell profile from volume data. Error bars represent standard deviation of the data. **(H)** 3D rendering. Two sample cells were considered to demonstrate the 3D rendering. Top panel shows the YAP/TAZ dKO and the bottom panel shows the LATS1/2 dKO. **(I)** Sample

profile for two cell lines. Top panel shows YAP/TAZ dKO and bottom panel shows LATS1/2 dKO. Shaded area is median 50%. **(J)** Cell shape comparison. Left panel shows the cell height distribution as a function of the radial distance from the cell's center of mass (volume in this case). Right panel shows the comparison when scaled by volume. The original and volume normalized apical cell shapes with the median height function (solid lines) and best-fit spherical cap (dashed lines); see Materials and methods for details on cap fitting. **(K)** Volume difference is not explained by cell shape. Top panel shows volume-normalized median cell height distributions across each ensemble with the indicated KO in red and HEK 293 in gray. Shaded area is median 50%. Only the LATS1/2 dKO shows a significant difference in 3D apical shape. ***, $P < 0.005$; ****, $P < 0.001$.

expression, leads to a larger contractile force. If the pressure gradient across the cortex were constant, one way to balance that larger contractile force would be to increase cell volume and decrease the curvature while maintaining the same shape. Thus, we sought to examine how cell shape varies with YAP/TAZ activity independently of cell volume and examined the 3D shape where the apical surface was reconstructed from the epifluorescent images used to calculate volume (Fig. 3, G and H) and normalized by cell volume (Fig. 3 I). We examined both the raw height profiles (Fig. 3 J) as a function of the distance from the center of each cell as well as the fitted spherical caps (Fig. S3 F). We found that there was no consistent trend in cell shape with increasing YAP/TAZ activity. The YAP/TAZ dKO, YAP KO, TAZ KO, and parental line (HEK 293A) were all found to be remarkably self-scaling. Despite having substantially different volumes, these four cell lines all had similar height profiles. It is interesting to note, however, that the LATS1/2 dKO does not exhibit the same shape, spreading more than the others (more "pancake-like"). Thus, the role the Hippo pathway and YAP/TAZ activity may play in cell shape regulation alone cannot explain the variations in volume observed across the CRISPR KOs.

### Cell volume regulation by YAP/TAZ is independent of mTOR activity

Another possible explanation for the observed cell volume increase with increasing YAP/TAZ activity is from the potential crosstalk between the Hippo and mTOR pathways. The Hippo pathway has been reported to modulate the mTOR pathway under certain conditions. Previous work (Tumaneng et al., 2012) has shown that in mouse tissue overexpression of YAP leads to the up-regulation of AKT (protein kinase B) through tumor suppressor PTEN (phosphatase and tensin homolog), and thus activates mTORC1/2 and its downstream components. Overexpression of YAP also increased the level of phosphorylation of both S6K Thr 389 and AKT Ser 473 in tissue. As mTOR has been described as a major regulator of mammalian cell size due to its relationship with amino acid import and protein synthesis (Fingar et al., 2002; Yang and Guan, 2007; Lloyd, 2013), it is natural to ask whether on the single-cell level the regulation of cell volume by the Hippo pathway is mediated through crosstalk between Hippo and mTOR. If YAP/TAZ activity also modulates mTOR activity on the single-cell level, it may explain the observed cell volume variation in Hippo pathway KOs. To explore this potential crosstalk between YAP/TAZ and the mTOR pathway, we first inhibited mTOR using rapamycin and replicated the previously published effect of rapamycin on cell size (Fingar et al., 2002; Fig. S4, A–C). After 4 h of treatment, mTOR activity was diminished, as reported by pS6 expression using qIF (Fig. 4, A and B). However, cell volume did not change significantly

after 4 h. Instead, a noticeable cell volume decrease of 28.9% occurred after 72 h, close to the range previously reported (Fingar et al., 2002). In addition, we found that under mTOR inhibition, YAP/TAZ activity remained unchanged, suggesting that mTOR is not an upstream regulator of YAP/TAZ (Fig. S4, A, B, D, and E).

Next, we sought to characterize mTOR activity (reported to be involved in protein production) in all Hippo pathway KOs, as well as the total cell protein content and cell protein synthesis rate. Total cell protein content is measured using the total fluorescence from cells stained with a succinimidyl ester dye (Kafri et al., 2013). This measurement has already been reported to be well correlated with measurements of dry mass by quantitative phase microscopy (Kafri et al., 2013). The cell protein synthesis rate is measured using the SUnSET method (Schmidt et al., 2009). By treating cells with low-concentration puromycin and staining puromycin-labeled premature peptides, we quantified the rate of protein synthesis in single cells by assessing the qIF signal of puromycin-labeled peptides within the cytoplasm. We found that although there is major change in YAP/TAZ expression throughout these cell lines (Fig. 4 D), mTOR activity, as measured by total pS6, remained fairly constant (Fig. 4 E), further ruling out crosstalk between these pathways at the single-cell level. We found no change in total cell protein content across five cell lines. The cell protein synthesis rate was also generally constant, with LATS1/2 dKO showing a slight increase.

Finally, we asked whether mTOR or Hippo pathways are independent in their regulation of cell volume and whether they have a synergistic effect. We found that when inhibiting mTOR activity with rapamycin in all Hippo pathway KOs, there was a general trend of obtaining additional volume reduction to what we had already seen in the Hippo KOs. Only the TAZ KO showed no significant volume reduction after mTOR inhibition. These results suggest that under the conditions tested, Hippo and mTOR have a synergistic effect in their regulation of cell volume and act essentially independently.

### YAP, but not TAZ, influences cytoplasmic pressure and impacts volume

Our cell volume and cell protein content data in Fig. 4 suggest that the cell volume is not directly proportional to cell protein content. Therefore, how cytoplasmic components determine the physical volume of the cell remains unexplained. The answer to this question will likely open avenues to understanding cell growth regulation. Toward this, we also measured the cell cytoplasmic pressure in these five cell lines (Fig. 4 K) using the servo-null system (Petrie and Koo, 2014). Results show that YAP, but not TAZ, influences cell cytoplasmic hydraulic pressure. Knocking out YAP reduces the pressure from 1 kPa to ~500 Pa.
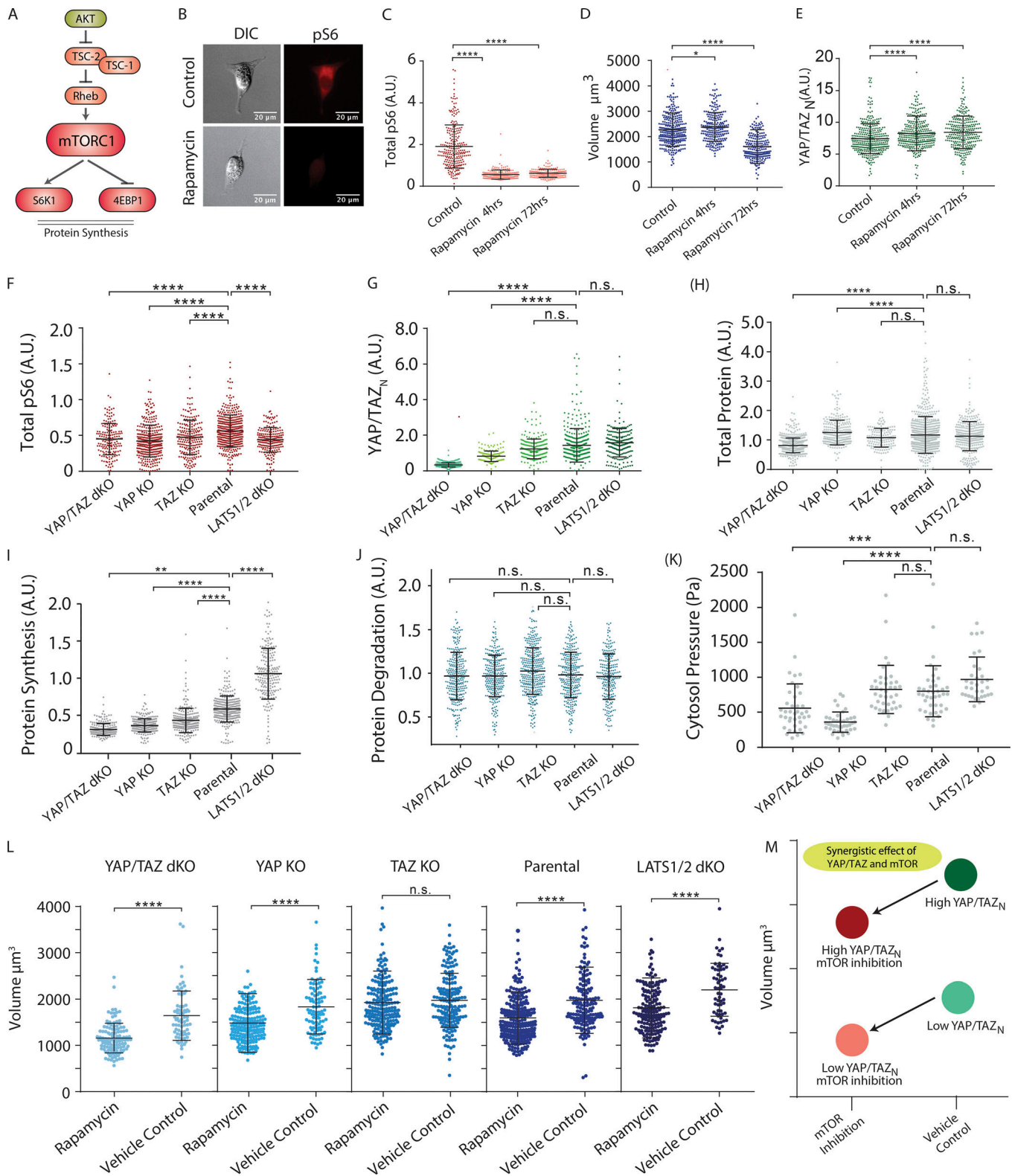
Figure 4. **Volume differences across Hippo pathway KOs are independent of the mTOR pathway. (A)** mTOR pathway and cell volume. Description of the key elements of the pathway. **(B)** Sample images of control cells and rapamycin treatment. Left two images show sample HEK 293A cells from control experiment, whereas two right images show sample cells after rapamycin treatment. **(C)** mTOR inhibition confirmation via qIF. Expression of ribosomal activity reported via qIF of ribosomal protein pS6 ($N_{Control}$ = 248, $N_{Rapamycin-4hours}$ = 196, $N_{Rapamycin-72hours}$ = 178). **(D)** Rapamycin treatment decreases cell volume after 72 h of treatment. Cell volume for control cells and rapamycin-treated cells at 4 and 72 h ($N_{Control}$ = 314, $N_{Rapamycin-4hours}$ = 224, $N_{Rapamycin-72hours}$ = 221). **(E)** mTOR inhibition does not affect YAP/TAZ activity. Nuclear YAP/TAZ expression measured via qIF ($N_{Control}$ = 354, $N_{Rapamycin-4hours}$ = 326, $N_{Rapamycin-72hours}$ = 296). **(F)** mTOR activity, measured as pS6 expression, does not change in Hippo pathway KOs ($N_{YAPTAZ dKO}$ = 177, $N_{YAP KO}$ = 336, $N_{TAZ KO}$ = 218, $N_{HEK 293A}$ = 406,

N$_{LATS1/2\ dKO}$ = 202). **(G)** Nuclear YAP/TAZ content by qIF. Hippo pathway activity was assessed by qIF in the parental line and all CRISPR KOs (N$_{YAPTAZ\ dKO}$ = 223, N$_{YAP\ KO}$ = 156, N$_{TAZ\ KO}$ = 287, N$_{HEK\ 293A}$ = 331, N$_{LATS1/2\ dKO}$ = 207). **(H)** Total protein content does not change with Hippo pathway KOs (N$_{YAPTAZ\ dKO}$ = 664, N$_{YAP\ KO}$ = 269, N$_{TAZ\ KO}$ = 150, N$_{HEK\ 293A}$ = 772, N$_{LATS1/2\ dKO}$ = 314). **(I)** Protein synthesis rate, measured using SUnSET, for Hippo pathway KOs. The synthesis rate shows increasing trend with increasing nuclear YAP content among the KO cell lines (N$_{YAPTAZ\ dKO}$ = 233, N$_{YAP\ KO}$ = 285, N$_{TAZ\ KO}$ = 257, N$_{HEK\ 293A}$ = 308, N$_{LATS1/2\ dKO}$ = 208). **(J)** Protein degradation, quantified by antibody targeting polyubiquitinated conjugate (N$_{YAPTAZ\ dKO}$ = 296, N$_{YAP\ KO}$ = 285, N$_{TAZ\ KO}$ = 362, N$_{HEK\ 293A}$ = 302, N$_{LATS1/2\ dKO}$ = 248). **(K)** Cytoplasmic hydraulic pressure measure by the servo-null system. Three biological repeats were included (N$_{YAPTAZ\ dKO}$ = 40, N$_{YAP\ KO}$ = 40, N$_{TAZ\ KO}$ = 40, N$_{HEK\ 293A}$ = 40, N$_{LATS1/2\ dKO}$ = 33). **(L)** Cell volume comparison for Hippo pathway KOs before and after mTOR inhibition (N$_{YAPTAZ\ dKO\ -\ Control}$ = 70, N$_{YAPTAZ\ dKO\ -\ Rapamycin}$ = 115, N$_{YAP\ KO\ -\ Control}$ = 95, N$_{YAP\ KO\ -\ Rapamycin}$ = 193, N$_{TAZ\ KO\ -\ Control}$ = 176, N$_{TAZ\ KO\ -\ Rapamycin}$ = 206, N$_{HEK\ 293A\ -\ Control}$ = 154, N$_{HEK\ 293A\ -\ Rapamycin}$ = 258, N$_{LATS1/2\ dKO\ -\ Control}$ = 61, N$_{LATS1/2\ dKO\ -\ Rapamycin}$ = 169). Error bars represent standard deviation of the data. **(M)** Our results suggest a synergistic effect of YAP/TAZ and mTOR in cell volume control. Inhibiting mTOR uniformly decreases cell size in all YAP/TAZ KOs. n.s., P ≥ 0.05; *, P < 0.05; **, P < 0.01; ****, P < 0.001.

Knocking out LATS1/2, which increases YAP activity, increased the cytoplasmic pressure slightly. Fundamentally, the cytoplasmic hydraulic pressure is related to the excess osmotic pressure and is determined by a combination of cell ionic content, cell protein content, and cell contractility. Indeed, in previous work, we presented a model of cell osmotic pressure and volume regulation which showed that the cell volume is proportional to the cell protein content, but the proportionality constant depends on cell ionic regulation and contractility (Tao and Sun, 2015). Earlier, we observed that YAP KO cells lacked a visible mitotic swelling before cytokinesis. This implicates YAP as a possible regulator of cell ionic content, the increase of which can lead to an increase in cell water content and pressure. Therefore, there is a complex dependence of cell volume on cell protein and ionic content that warrants further exploration.

### Tension regulation through the G1/S checkpoint could explain cell volume variations

So far, we have demonstrated that all volume changes observed due to the modulation of YAP/TAZ activity are not explained by the role of YAP/TAZ in the regulation of the volumetric growth rate (Fig. 2), cell cycle duration (Fig. 3), cell geometry (scaled by volume; Fig. 3), or mTOR activity (Fig. 4). In previous work (Perez-Gonzalez et al., 2018), we discussed the relationships between YAP/TAZ, cortical tension, and volume. Here we go a step further to propose that the trend of increasing volume across the CRISPR KOs might be explained as a consequence of increasing cell tension, which in turn increases YAP/TAZ activity (Fig. 5, A and B). As previously published, we propose that the distribution of cortical tension, maintained through phosphorylated myosin-mediated active contraction, determines the force balance at the cortex, thereby determining the volume of the cell. To validate this framework for the Hippo pathway KOs, we first measured pMLC expression and found that, as expected, it was positively correlated with YAP/TAZ expression and activity (Fig. 5 D), while its distribution in the cell apical cortices remained fairly constant (Fig. S5, A–C). When comparing our measured values for pMLC and volume, we found that pMLC was an excellent proxy for cell volume (Fig. 5 F). We went on to characterize the pMLC expression for cells identified to be in G1 by Hoechst labeling for each cell line and found that the G1 exit value for pMLC (the value bounding 90% of cells in G1) was again correlated with the average cell volume of the cell line (Fig. S5 A). We hypothesize that YAP/TAZ and pMLC may be influencing a G1/S cell cycle checkpoint. To support the existence of

such a checkpoint, which has recently been motivated in monolayers (Uroz et al., 2018) for isolated HEK single cells, we measured cell cycle progression in a synchronized population under pMLC inhibition with the Rho-associated, coiled-coil containing protein kinase (ROCK) inhibitor Y27632. We took an asynchronous population (Fig. 5 G), performed mitotic shake-off detachment to obtain dividing cells, and let this population progress to G1 (Fig. 5 H). We then compared the evolution of this population over time with (Fig. 5 J) and without (Fig. 5 I) the addition of Y27632. We found that with the addition of Y27632, there were significantly fewer cells progressing from G1 to S. Recently, it was shown that cell cytoskeletal tension impacts the association of the SW1/SNF complex with YAP/YAZ, which inhibits transcriptional activity of nuclear YAP/TAZ (Chang et al., 2018). This result, in combination with our observation, suggests that pMLC activity and cell tension together with YAP/TAZ activity are involved in the determination of this cell cycle checkpoint.

## Discussion

Our data show that YAP/TAZ are involved in regulating single-cell volume and provide insights into how YAP/TAZ is potentially regulating cell size. We found cell birth volume and division volume to be dependent on YAP/TAZ activity, with higher YAP/TAZ activity leading to larger cell size. We validated (Plouffe et al., 2018) that cell cycle duration decreases with increasing YAP/TAZ activity, and also observed that the volumetric growth rate $dV/dt$ increases with YAP/TAZ activity.

Neither the observed dependence on YAP/TAZ activity for the regulation of cell cycle duration nor any potential modulation of the volumetric growth law is able to explain the volume variation observed. We additionally considered the possibility that this phenomenon is purely mechanical, owing to the potential role of YAP/TAZ in the regulation of cell shape; however, we found four of five of the cell lines that we investigated to exhibit self-similar shapes, negating this hypothesis as well. Finally, we sought to establish YAP/TAZ as either directly up- or downstream of mTOR, a known regulator of cell volume and instead we found them to act both independently and synergistically under the conditions tested in this study. Intriguingly, we found that YAP, and not TAZ, seems to influence the cytoplasmic hydraulic pressure, which may contribute to mechanotransduction function of YAP as well as cell volume regulation.

Having exhausted these possible explanations, we aimed to propose a novel mechanism implicating the role of YAP/TAZ
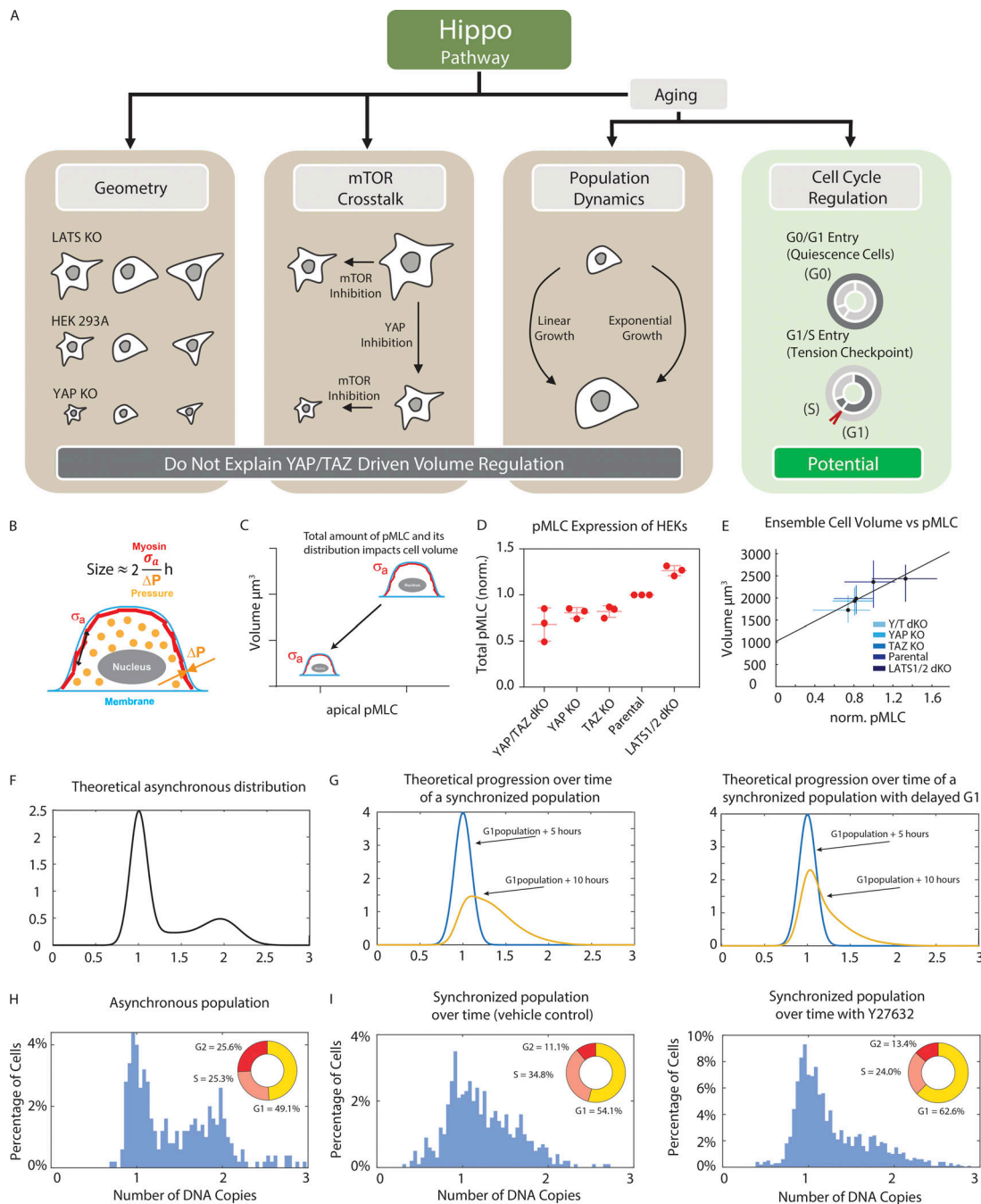
Figure 5. **YAP/TAZ may be modulating cell volume in combination with cytoskeletal tension during cell cycle progression. (A)** Possible explanations for the mechanism by which the Hippo pathway regulates cell volume. Hippo affects cell geometry: excluded (does not explain cell volume variation). Cells appear to self-scale their shape when YAP and/or TAZ are knocked out. Hippo cross-talk with mTOR: excluded. In low amino acid conditions, this cross-talk is an essential component of both signaling pathways (Tumaneng et al., 2012); however, under the experimental conditions tested for this study, mTOR and Hippo are observed to act independently. Hippo affects cell volume by influencing cell growth rate and cell cycle distribution: plausible. Potential changes in growth rate caused by perturbing YAP/TAZ fails to explain cell volume regulation; however, cell cycle regulation including modulation of G1/S checkpoint may explain cell volume variation. **(B)** Cartoon showing relationship between volume and cortical tension, $\sigma_a$. **(C)** Cartoon showing expected relationship between apical pMLC and volume. **(D)** qIF measurement of pMLC expression changes among HEKs. Each data point is a biological repeat. Each point is an average of 100–200 cells. **(E)** Linear relationship between average cell volume and average cell pMLC. Error bars represent standard deviation of the data. **(F)** Theoretical asynchronous distribution of cell DNA content within a population. See Materials and methods. **(G)** Theoretical prediction of DNA distribution over the course of the experiment. See Materials and methods. **(H)** Progression from G1 after shake-off synchronization in M. Left panel shows the synchronized population (blue) versus the population evolving over time (yellow). Right panel shows the synchronized population (blue) and the population evolving over time when G1 progression is delayed (yellow). **(I)** asynchronous cell cycle distribution for HEK 293A. **(J)** Y27632 assay. Left panel shows how the cells progress from a synchronized G1 population with vehicle control (DMSO). Right panel shows how the cells progress from a synchronized G1 population with Y27632. Insets show the fraction of cells in each cell cycle phase.

in the regulation of cortical tension and thus cell volume throughout the G1/S checkpoint. We established a strong positive correlation between YAP/TAZ activity, cell volume, and cell tension and went on to validate the importance of cell tension through the navigation of the G1/S checkpoint in isolated HEK single cells by demonstrating that ROCK and myosin inhibition delays or prohibits the exit of G1 and entrance to S. We posit that YAP/TAZ modulates cortical tension, and thus cell volume during this transition, further impacting volume at birth and division. Recently, it was shown that the SWI/SNF complex can inhibit YAP/TAZ transcriptional activity in the cell nucleus in a cell tension–sensitive manner (Chang et al., 2018), and YAP/TAZ nuclear import is sensitive to mechanical forces (Elosegui-Artola et al., 2017). Our findings suggest that tension sensitivity of YAP/TAZ ultimately translates to differences in cell cycle progression, providing a novel explanation of cell size control in different mechanical environments.

## Materials and methods

### Cell culture
HEK 293A cells were a gift from Kun-Liang Guan (University of California, San Diego, San Diego, CA), as were CRISPR KOs on the Hippo pathway. LATS1/2 dKO was generated as detailed in Meng et al. (2015), whereas YAP KO, TAZ KO, and YAP/TAZ dKO were generated as detailed in Plouffe et al. (2018). The cells were cultured in DMEM (Corning) supplemented with 10% FBS (Sigma-Aldrich) and 1% antibiotic solution (10,000 units/ml penicillin and 10,000 μg/ml streptomycin [P/S]; Gibco) at 37°C and 5% $CO_2$.

### Cell size assessments
Cells were sized and counted with a Coulter Counter (Multisizer 3; Beckman Coulter) using an orifice size of 50 μm and a lower size measurement limit of 1 μm. In addition to the Coulter Counter measurements, cells were alternatively used by flow cytometry with the following protocol. First, cells were resuspended in DMEM with 10% FBS and 1% P/S. The sample was centrifuged at 1,500 rpm for 5 min. The supernatant was removed, and the cells were resuspended in 5 ml of PBS in the tube. Cells were counted using a hemocytometer. We centrifuged 1 ml with 500,000 cells at 1,500 rpm for 5 min. We removed the supernatant and resuspended cells in 500 μl of ice-cold PBS. We added 4.5 ml of ice-cold 70% ethanol in 0.5-ml increments, vortexed in every iteration, and then placed the cells on ice or in a freezer overnight. We centrifuged again at 1,500 rpm for 5 min to remove the supernatant and resuspended the cells in 1 ml PBS. To generate a nuclear signal, we pipetted 10 μl of stock Hoechst 33342 (final Hoechst concentration 100 μg/ml) and incubated the cells for 60 min. Finally, we transferred the mix into a Corning Falcon Test Tube with Cell Strainer Snap Cap (i.e., filter) and measured the fluorescence intensity using a SH800S Cell Sorter.

### Microfluidic device fabrication
Silicon molds were fabricated using standard photolithography procedures. Masks were designed using AutoCAD and ordered from FineLineImaging. Molds were made according to the manufacturer's instruction for SU8-3000 photoresist. Two layers of photoresist were spin coated on a silicon wafer (IWS) at 500 rpm for 7 s with acceleration of 100 rpm/s, and at 2,000 rpm for 30 s with acceleration of 300 rpm/s, respectively. After a soft bake of 4 min at 95°C, UV light was used to etch the desired patterns from negative photoresist to yield feature heights that were ~15 μm. The length of the channels is 16.88 mm and the width is 1.46 mm.

A 10:1 ratio of PDMS Sylgard 184 silicone elastomer and curing agent were vigorously stirred, vacuum degassed, poured onto each silicon wafer, and cured in an oven at 80°C for 45 min. Razor blades were then used to cut the devices into the proper dimensions, and inlet and outlet ports were punched using a blunt-tipped 21-gauge needle (McMaster Carr; 76165A679). The devices were sonicated in 100% IPA for 15 min, rinsed with water, and dried using a compressed air gun.

50-mm glass-bottom Petri dishes (FlouroDish Cell Culture Dish; World Precision Instruments) were cleaned with water and dried using a compressed air gun. The Petri dishes and PDMS Sylgard 184 devices were then exposed to oxygen plasma for 1 min for bonding. Finally, the bonded devices were placed in an oven at 80°C for 45 min to further ensure bonding.

### Cell volume measurements
Microfluidic chambers were exposed to 30-s oxygen plasma before being incubated with 50 μg/ml of type I rat-tail collagen (Corning; 354236) for 1 h at 37°C. The chambers were washed with 1× PBS before ~50,000 cells were injected into them. The dishes were then immersed in medium to prevent evaporation. The cells were seeded with 0.1 μg/ml of Alexa Fluor 488 Dextran (molecular weight 2,000 kD; Thermo Fisher Scientific), allowed to adhere in the incubator at 37°C with 5% $CO_2$ and 90% relative humidity, and then imaged within 12 h.

The cells were imaged using a Zeiss Axio Observer inverted, wide-field microscope using a 20× air, 0.8-NA objective equipped with an Axiocam 560 mono charged-coupled device camera. The microscope was equipped with a $CO_2$ Module S (Zeiss) and TempModule S (Zeiss) stage-top incubator (Pecon) that was set to 37°C with 5% $CO_2$ for long-time imaging. Differential interference contrast (DIC) microscopy was used to accurately capture the cell area and shape, and epifluorescent microscopy was used to measure volume. Individual cells were traced using the algorithm below.

Cell contours were segmented from the DIC and epifluorescence (volume) channels. First, a rough contour is generated from a smoothed copy of the epifluorescence channel, where pixels darker than the background intensity are identified. Next, a measure of the local contrast of the DIC channel (here high-contrast regions are identified) is used to expand the contour to include small features (small lamellipodia, etc.) that have low contrast in the volume channel and may be missed. This expanded contour is used to identify the cell boundary. Inner and outer annuli are created by dilating this contour 10 and 25 pixels away from the cell (inner boundary shown in Fig. S1 A). The mean fluorescence intensity of the pixels between inner and outer annulus, or mean background intensity $I_{annulus}$, is related

Perez-Gonzalez et al.
YAP and TAZ regulate cell volume

Journal of Cell Biology    3482
https://doi.org/10.1083/jcb.201902067

to the total channel height. The volume boundary, shown as a purple line in Fig. S1 B, is created by dilating the cell contour 20 pixels away from the cell. The local fluorescence intensity enclosed by the volume boundary $I_V$ corresponds to the local height above the cell ($h_2$, shown in Fig. 1 A). The volume of the cell is then calculated as follows:

$$V = \text{Channel Height} \sum_{\text{pixels within volume boundary}} \left(1 - \frac{I_V}{I_{Annulus}}\right)\delta A.$$

Every experiment on cell volume was repeated at least three times with three technical repeats corresponding to the three individual channels in the microdevice. Experiments in glass gave ≥50 single cell measurements. Softer substrates yielded smaller datasets per measurement. The sample size for volume measurements was kept at >200 single cells, with the exception of birth and peak volume (Fig. 1 N). This was done to get a normal distribution for each complete dataset.

### Intracellular pressure measurements
Direct measurements of intracellular pressure were performed using the 900A micropressure system (World Precision Instruments) according to the manufacturer's instructions as described previously (Petrie and Koo, 2014). Briefly, a glass micropipette with a 0.5-µm-diameter tip (World Precision Instruments) was filled with a 1-M KCL solution, placed in a microelectrode holder half-cell (World Precision Instruments), and connected to a pressure source regulated by the 900A system. The calibration chamber (World Precision Instruments) was filled with 0.1 M KCl and connected to the 900A system, and the resistance of each microelectrode was set to 0 and attached to a MPC-200 micromanipulator (Sutter Instrument) within an environmental chamber (37°C and 10% CO$_2$) on an LSM 700 microscope (Zeiss). To measure intracellular pressure, the microelectrode was driven at a 45° angle into the cytoplasm, maintained in place for ≥5 s, and removed. The pressure measurement was calculated as the mean pressure reading during this time interval. The experimenters were blinded to the identity of the five cell lines to eliminate potential bias.

### Dye endocytosis comparison
To check whether dye endocytosis contributes to the cell volume signal in the microfluidic volume measurements, YAP/TAZ dKO, YAP KO, TAZ KO, HEK-293A, and LATS1/2 dKO cells were seeded into a 24-well plate, and 0.1 µg/ml of Alexa Fluor 488 Dextran (molecular weight 2,000 kD; Thermo Fisher Scientific) dye was added to the cell culture for durations of 1, 2, 5, and 8 h. After incubation with dye for these varying durations, the wells were washed thoroughly three times (10 min for each wash) with DMEM (10% FBS and 1% P/S). We then imaged and quantified the fluorescent intensity ratio between each cell and the background.

### Immunofluorescence
Immunofluorescence was performed as described previously (Aifuwa et al., 2015). Briefly, cells were seeded at single-cell density (12,000 cells/cm² for all HEK 293A cell lines) for 6 h

and then fixed with 4% PFA (100503-917; VWR) for 10 min. Samples were then rinsed three times with 1× PBS. 0.1% Triton X-100 (T8787; Sigma-Aldrich) dissolved in PBS was then added for 10 min, and the cells were washed three times with 1× PBS. The fixed cells were blocked with 1% BSA (A7906; Sigma-Aldrich) for 1 h at room temperature. Primary antibodies were incubated overnight in 1% BSA. Antibodies included YAP 63.7 (1:100, mouse; SC/101199), phospho-myosin light chain 2 Thr18/Ser19 (1:100, rabbit; #3674; Cell Signaling Technology), and pS6 (1:1,000, rabbit; #5364; Cell Signaling Technology). The next day, the dishes were rinsed three times with 1× PBS and incubated for 2 h with the following secondary antibodies: Alexa Fluor 488 (mouse) and 568 (rabbit). DNA was stained using 20 µg/ml Hoechst 33342. In addition, in combination with the Hoechst 33342, we used a succinimidyl ester dye (SE-A647) that reacts with lysil groups as reported by Kafri et al. (2013).

Wide-field microscopy using the setup described above was used to measure the total pMLC, YAP/TAZ, pS6, DNA content, and total protein content of the cells. To obtain spatial information about pMLC, we used a Zeiss LSM 800 confocal microscope equipped with a 63× oil-immersion, 1.2-NA objective. A 567-nm laser was used to image the stained cells. Images were acquired with a resolution of 1,024 × 1,024 pixels, which gives a field of view of 10,485.76 µm². We imaged the cells with confocal image stocks of total thickness of 20 µm to cover the entire height of the cells. Confocal image slices were spaced 2 µm apart, and the pinhole size was 1 µm.

For each fluorescence image, we subtracted the pixel intensities with mean background intensity. A binary mask was generated based on the pixel intensities of fluorescence image (the pixel intensities within the cell region are much higher than elsewhere), where pixels within the cell/nucleus region are marked with 1 and pixels outside the cell/nucleus are marked with 0. By multiplying the binary mask with actual fluorescence images, we identified all the pixel values within the cell/nucleus. The total intensities within the cell/nucleus boundary were calculated by summing up all the intensity values. The cell and nucleus boundary were then traced by Matlab routine "bwboundaries." Every traced region with a total area of ≤1,500 square pixels was considered as debris or cell fragments and therefore ignored.

We used the pMLC channel to generate the binary mask for the cell. The traced boundary was then dilated 15 pixels away from the cell, to capture all the scattered light from epifluorescence image. The binary mask for the cell nucleus was generated based on Hoechst channel. No dilation was made on the nucleus mask, to avoid overestimation of total nucleus YAP. We multiplied the nucleus mask with every cell mask, to exclude all the nuclei from other cells within the same field of view. The traced boundary is shown in Fig. S1 B.

For confocal z stacks, the basal layer of the cell was identified when clear stress fibers were seen (example in Fig. S5 B). All stacks below the basal layer were neglected. We identified the first apical slide when the stress fibers disappeared. The traced boundary of every apical slide was dilated 5 pixels (~1 µm) inside the cell, to mark the inner boundary of the cortical layer. Fig. 5 D shows that pMLC are mainly cortical, except for the

Perez-Gonzalez et al.
YAP and TAZ regulate cell volume

Journal of Cell Biology
https://doi.org/10.1083/jcb.201902067

3483

basal layer, where some stress fibers can be seen. Therefore, the pMLC within the cell cytoplasm is minimal compared with cortical pMLC.

Every experiment was repeated two times with two technical repeats. In addition, each technical repeat consisted of ≥100 single-cell measurements (except for confocal measurements). The sample size for qIF aimed for ≥200 single cells. This dataset size was targeted to get a normal distribution for each complete dataset. Finally, no single cells were excluded during the analysis of these datasets. The only cells excluded were those forming clusters.

## Cell protein synthesis measurement

The SUnSET method (Schmidt et al., 2009) was applied as a measurement of single-cell protein synthesis rate. The HEK cells were seeded at 20,000 cells/ml in a 24-well plate for 4 h in the incubator with DMEM (10% FBS and 1% PS), and then treated with 10 µg/ml puromycin (P8833; Sigma-Aldrich) diluted in Dulbecco's PBS for 10 min in the incubator. Cells were fixed using 4% PFA right after puromycin treatment and stained according to the immunofluorescence protocol described above. Anti-puromycin antibody, clone 12D10 (MABE343 EMD, Millipore; host species: mouse), was used at a ratio of 1:1,000 in BSA as the primary antibody solution, and mouse Alexa Fluor 488 was used at a ratio of 1:1,000 in Dulbecco's PBS as the secondary antibody solution.

## Western blotting

Cells were lysed in SDS sample buffer (50 mM Tris, pH 6.8, 2% SDS, 0.025% bromophenol blue, 10% glycerol, and 5% β-mercaptoethanol) and boiled for 5 min. Proteins were separated on 8–10% Bis-Tris polyacrylamide gels. Immunoblots were performed as previously described (Meng et al., 2015). Antibodies for Lats1 (#9153) and Lats2 (#5888) were purchased from Cell Signaling Technology. YAP 63.7 (sc-101199; host species: mouse) was purchased from Santa Cruz (this antibody recognizes both YAP and TAZ). Vinculin (V9131) was purchased from BD Biosciences.

## Microscope image acquisition

For both cell volume measurements via the FX method and the immunofluorescence assays, the cells were imaged using a Zeiss Axio Observer inverted, wide-field microscope using a 20× air, 0.8-NA objective equipped with an Axiocam 560 mono charged-coupled device camera. The microscope was equipped with a $CO_2$ Module S (Zeiss) and TempModule S (Zeiss) stage-top incubator (Pecon) that was set to 37°C with 5% $CO_2$ for live cell imaging. For imaging of immunofluorescence assays, the samples were imaged under room temperature and $CO_2$. For cell volume measurements, the imaging medium was DMEM with 10% FBS and 1% P/S, and Alexa Fluor 488 dye was used as the fluorochrome. For immunofluorescence assays, the imaging medium was PBS; and Alexa Fluor 488 and 568 were used as the fluorochromes. ZEN 2 Software (Zeiss) was used as the acquisition software. Matlab 2018a (MathWorks) was used for image analysis subsequent to data acquisition. Boundary tracing was applied to acquire the boundary of the cell. The cell and nucleus boundary were traced by Matlab routine "bwboundaries." Every

traced region with total area of ≤1,500 square pixels is considered debris or cell fragments and therefore ignored.

## Mathematical predictions of cell volume distributions

We identified within the five cell lines observed that the mean volume of each population increases with increasing YAP/TAZ activity in that population. This is largely because the birth and division volumes increase across the populations; however, we also explored ways in which the mean ensemble volume could change while the birth and division volumes remain unchanged. To do so, we used the von Foerster equation, which computes the distribution of cells with age-related (cell age is defined as the time that has elapsed since the last cell division) quantities including volume:

$$\frac{\partial n}{\partial t} + \frac{\partial n}{\partial a} = \lambda,$$

where $n(a,t)da$ is the number of cells in the distribution with ages (or time since birth) between $a$ and $a + da$ and $t$ is the chronological time. $\lambda$ represents the loss rate, the rate at which cells leave the ensemble. The number density of cells at age $a + da$ at time $t + dt$ is simply the number density of cells of age $a$ at time $t$ minus those that left the ensemble due to cell division, etc. Considering $\lambda$ to represent only loss due to mitosis, we may write the boundary condition

$$n(0,t) = 2\int_0^\infty \lambda(a)n(a,t)da,$$

which illustrates that the number of cells at age 0 is simply twice the number of cells that just divided. We may further rewrite $\lambda$ in terms of the division time distribution, $w(a)$, which is also the cell cycle duration distribution, the amount of time it takes for a cell to divide (Stukalin et al., 2013). The probability of undergoing mitosis per unit time at age $a$ is the ratio of the population of cells observed to divide at age $a$ over the fraction of cells which have matured to age $a$ without yet dividing. Given only $w(a)$, one may then solve for the bulk growth rate of the mitotic population $b$ using the following expression (see Stukalin et al. [2013] for a derivation):

$$1 = 2\int_0^\infty \exp(-ba)w(a)da,$$

where the cell number distribution is assumed to follow the form $n(a,t) = g(a)e^{bt}$ and the age distribution is explicitly

$$g(a) = 2b\exp(-ba)\left[\int_a^\infty w(a')da'\right].$$

In previous work (Rochman et al., 2018), we showed the age distribution to be self-scaling. In other words, the probability of observing a cell of scaled age $a/\mu$, where $\mu$ is average duration of the cell cycle, is independent of $\mu$. While there is some dependence on the coefficient of variation (CV) of the cell cycle duration distribution, given this self-scaling, one may approximate the cell cycle completion distribution, that is, the probability that a cell has completed $100 \times x\%$ (where $x$ is the cell completion fraction) of its cycle at the time observed as the conserved

function (Fig. S3 B) $\rho(x) = 2\ln(2)\exp[-\ln(2)x]$, which may be validated through simulation.

This expression may be used to calculate the volume distribution for an ensemble (in principle, any observable DNA content; for example, Fig. 3 E) given $P(V|x)$, the conditional probability that the volume is some value given that the cycle completion fraction is $x$:

$$\rho(V) = \int_0^1 P(V|x)\rho(x)dx.$$

This expression clarifies the idea that the mean volume can change either by changing $P(V|x)$ (e.g., changing the birth and division volume) or by changing $\rho(x)$. Assuming $\rho(x)$ is conserved, the only possibility that remains is to change $P(V|x)$. This still does not require changing the birth/division volume. In particular, we examined whether the difference between a linear growth law, an exponential growth law:

$$P(V|x) = N\left\{V, V_{Birth}\exp\left[\ln\left(\frac{V_{Division}}{V_{Birth}}\right)x\right], y\right\},$$

$$N[V, V_{Birth} + (V_{Division} - V_{Birth})x, y],$$

or a hypothetical logarithmic growth law:

$$P(V|x) = N\left\{V, V_{Birth}\ln\left[\exp\left(\frac{V_{Division}}{V_{Birth}}\right)x\right], y\right\},$$

where $N(V,x,y)$ indicates the normal distribution

$$N(V, x, y) = \frac{1}{\sqrt{2\pi(xy)^2}}\exp\left[-\frac{(V-x)^2}{2(xy)^2}\right],$$

with a mean of $x$ and a CV of $y$, could result in measurably different volume distributions. We examined the linear and exponential cases in the main text (Fig. 3 C) and found the differences in the predicted volume distributions to be negligible. Here we provide an additional investigation of all three cases. Differing cell cycle durations do not impact the final volume distributions (the age distributions for the examples shown in the main text are included in Fig. S3 A for completeness) and will be ignored.

As cells roughly double over the course of the cell cycle, we consider cells obeying logarithmic (dotted line), exponential (dashed line), and linear (solid line) growth laws increasing in size from one to two (red curves) and two to four (black curves) arbitrary units (Fig. S3 C). The resulting volume distributions depend additionally on the choice of CV: the larger the CV, the greater the heterogeneity of the population. For CVs >0.15, which replicate the shape of the experimentally observed volume distributions and are displayed in the main text, the choice of growth law only modestly impacts the final volume distributions (Fig. S3 D). For smaller CVs, however, the effects are more dramatic (Fig. S3 E). In this small-CV regimen, the logarithmic growth law produces a significantly right-weighted volume distribution, with cells spending a greater portion of the cell cycle at a larger volume. Similarly, the exponential growth law is left skewed and the linear growth law takes on the shape of the cell cycle completion distribution (Fig. S3 B).

We may further use this framework to arrive at an approximation for the average ensemble volume in terms of the cell cycle duration $\tau$ and the volumetric growth rate

$$\frac{dV}{dt}$$

alone. The result is similar for both exponential and linear cases, so we will assume a linear growth law for simplicity. Now we may consider that a cell roughly doubles over the course of the cell cycle, implying

$$V_{Division} = V_{Birth} + \tau\frac{dV}{dt} = 2V_{Birth},$$

and thus

$$\bar{V} = \int_0^1\left[V_{Birth}(1+x)\right]2\ln(2)\exp[-\ln(2)x]dx = \frac{1}{\ln(2)}V_{Birth}$$

$$= \frac{1}{\ln(2)}\tau\frac{dV}{dt} \approx \frac{3}{2}\tau\frac{dV}{dt}.$$

## 3D cell shape reconstruction

We sought to determine if increasing YAP/TAZ activity impacted cell shape. From previous work (Perez-Gonzalez et al., 2018), we know that cell geometry plays a major role in the force balance at the cell surface and therefore the cell shape. First a traditional 2D projected shape was compared across the cell lines investigated, with little variation observed due to the relatively nonprotrusive behavior of the parental cell line HEK 293A. Next, we examined 3D shape where the apical surface was reconstructed from the epifluorescent images used to calculate volume. To collapse self-scaling (similar) cell shapes, the surfaces were normalized by cell volume (x, y, and z position were all scaled by the cubed root of the volume) so that each normalized surface enclosed a volume of 1 arbitrary unit. Being largely symmetrical, the cell lines investigated were found to be well approximated by spherical caps. The volume for a cap is given by the expression

$$V = \frac{\pi r^3\beta^2}{3}(3-\beta),$$

where the height of the cap is $r\beta$. The height distribution for each cell as a function of the distance from the center of mass of the cell (in this case center of volume) was calculated. A median height curve was then constructed, and the best-fit $\beta$ and $r$ were chosen for that curve. The 25th and 75th percentiles in $\beta$ were identified (representing the most pancake-like and the most hemispherical, respectively). We found that there was no consistent trend in cell shape with increasing YAP/TAZ activity. The YAP/TAZ dKO, YAP KO, TAZ KO, and parental line (HEK 293A) were all found to be self-scaling (despite volume variation, the cell shapes were found to be similar when viewed as collective ensembles). It is interesting to note, however, that LATS1/2 dKO does not exhibit the same shape, with a significantly smaller mean $\beta$ (more pancake-like; Fig. S3 F).

## G1/S cell size checkpoint

Another potential avenue through which changes in YAP/TAZ activity could be regulating cell volume is the specification of a

G1/S cell size checkpoint. We looked at the birth volume, division volume, growth rate, DNA distribution, and pMLC data collected to determine if this possibility was self-consistent with previous measurements. We have observed the DNA distributions to be unchanged across the cell lines investigated, indicating that the fraction of the cell cycle spent in G1 is likely to be conserved: $t_{G1}/t_{Cycle} \equiv C$. Additionally, we found no significant dependence on cell cycle phase (e.g., G1, S, G2) for the volume growth rate, indicating the growth curve may be well approximated (within one doubling) with a linear function

$$V = V_{Birth} + \frac{V_{Division} - V_{Birth}}{t_{Cycle}} t.$$

Thus, we may expect

$$\frac{V_{G1} - V_B}{V_D - V_B} \equiv C.$$

Noting that the cell roughly doubles in volume over the course of the cell cycle, this may be simplified to be

$$\frac{V_{G1}}{V_B} \equiv C'.$$

We then found the lowest value of pMLC below which 90% of the G1 cells in each population lie, $PMLC_{G1}$. We found mean $V_B$ to increase ~30% from the smallest population, YAP/TAZ dKO, to the largest population, LATS1/2 dKO; however, $PMLC_{G1}$ increased twofold (Fig. S5 A). This implies that the correspondence between pMLC and volume cannot be simply $V = \alpha pMLC$ but rather $V = \gamma + \alpha pMLC$ with a positive $\gamma$. We then found the best-fit line for the mean volume across each population as a function of the mean pMLC and confirmed a positive $\gamma$ (Fig. 5 E). Thus, all data collected are consistent with the possibility of YAP/TAZ-dependent scaling of G1 checkpoint volumes across the cell lines examined.

We went on to probe the effect of cell tension on the G1 checkpoint volume through the use of ROCK inhibitor Y-27632. We found that the progression from G1 to S was delayed with the addition of Y-27632. These results may be interpreted to indicate a lengthening of the G1 duration. Seeking to compare the experimental DNA distributions obtained with those expected through a predicted lengthening of G1, we constructed the following theoretical framework.

At the beginning of the experiment, cells occupy some initial cell cycle completion distribution, $\rho(x)$ (where $x$ will be denoted the cell cycle "completion-fraction"), and cell cycle duration distribution, $w(a)$ (see Mathematical predictions of cell volume distributions). The cell cycle completion distribution may be propagated forward in time given the conditional probability of arriving at a new completion fraction given that a cell was at a preceding completion fraction at the previous time point. Assuming the time elapsed is sufficiently short so that no cell divides twice, the probability of arriving at completion fraction $y$ given a start at completion fraction $x$ takes one of two forms depending on whether a cell divides during the time step. For the case with no division occurring during the specified time step, this expression takes the form

$$P[y(t)|x]dy = w\left(\tau = \frac{\Delta t}{y - x}\right)d\tau.$$

The case with a single cell division occurring during the specified time step is

$$P[y(t)|x]dy = \left\{\int_0^\infty w\left[\tau = \frac{\Delta t - (1 - x)\tau_1}{y}\right]w(\tau_1)d\tau_1\right\}d\tau,$$

where $\tau_1$ is the duration of the completed cell cycle. The total conditional probability is not simply the sum of the two terms above, because the second term accounts for events during which the cell divides and thus are duplicated in the resultant distribution. Thus, the resultant distribution, $\rho_{\Delta t}(y)$, which is the cell cycle completion distribution at time $\Delta t$, is given by the following expression:

$$\rho_{\Delta t}(y) = A\left\{\begin{array}{l}\int_0^y w\left(\tau = \frac{\Delta t}{y - x}\right)\frac{d\tau}{dy}\rho(x)dx \\ +2\int_0^1\left\{\int_0^\infty w\left[\tau = \frac{\Delta t - (1 - x)\tau_1}{y}\right]w(\tau_1)d\tau_1\right\}\frac{d\tau}{dy}\rho(x)dx\end{array}\right\},$$

where $\rho(x)$ is the cell cycle completion distribution at time 0, and the constant $A$ indicates that this expression requires renormalization. While this result may be achieved numerically, artifacts and instability largely due to the inverse relationship between $y$ and $\tau$ make this cumbersome. Alternatively, the following approximation may be implemented:

$$\int_0^\infty w\left[\tau = \frac{\Delta t - (1 - x)\tau_1}{y}\right]w(\tau_1)d\tau_1 \sim w\left[\tau = \frac{\Delta t}{(1 + y) - x}\right].$$

While this is true for the case where $w(\tau) = \delta(\tau - \tau^*)$, it is not true in general; however, it is adequate for the purpose of this work, and this expression for the resulting distribution,

$$\rho_{\Delta t}(y) = A\left\{\begin{array}{l}\int_0^y w\left(\tau = \frac{\Delta t}{y - x}\right)\frac{d\tau}{dy}\rho(x)dx \\ +2\int_0^1 w\left[\tau = \frac{\Delta t}{(1 + y) - x}\right]\frac{d\tau}{dy}\rho(x)dx\end{array}\right\},$$

using this approximate, may be used.

While this expression may be used to propagate the cell cycle completion distribution forward in time, to make predictions about the distribution of cells residing in the cell cycle phases, G1, S, and G2, we need to specify the completion fraction at which each phase begins and ends. In principle, these may not be fixed quantities. For example, if a cell spends much more than the average amount of time in G2 in a given cycle, its daughter cells may spend less time in G1 to compensate. The model below does not include any potential mother–daughter correlations and simply assumes that G1, S, and G2 occupy constant fractions of the cell cycle across the population until acted upon by the drug, G1: $x \in [0, g_1]$, S: $x \in [g_1, s]$, and G2: $x \in [s, 1]$. The action of the drug is also simplified to be discrete. Before the drug is introduced, G1, S, and G2 are assumed to occupy constant fractions $g_1$, $s - g_1$, and $1 - s$ of the cell cycle. The moment the drug is introduced, these fractions are assumed to become

$$\frac{(1+\phi)g_1}{1+\phi g_1}, \quad \frac{s-g_1}{1+\phi g_1}, \text{ and } \frac{1-s}{1+\phi g_1},$$

and model a process by which the duration of G1 increases by a constant fraction φ and the durations of S and G2 are unchanged:

$$\text{G1: } x \in [0, (1+\phi)g_1];$$
$$\text{S: } x \in [(1+\phi)g_1, s+\phi g_1];$$
$$\text{G2: } x \in [s+\phi g_1, 1+\phi g_1].$$

The cell cycle completion distribution is thus modified after the action of the drug to become $\rho_\phi(x)$. The map between $\rho(x)$ and $\rho_\phi(x)$ is assumed to be a uniform dilation of the interval $[0, g_1]$ to $[0, (1+\phi)g_1]$ and a rigid translation of the intervals $[g_1, s]$ and $[s, 1]$ to the intervals $[(1+\phi)g_1, s+\phi g_1]$ and $[s+\phi g_1, 1+\phi g_1]$, respectively. In other words, cells in G1 experience a uniform dilation of the remaining portion of G1 they have yet to complete, while cells in S and G2 are unaffected until the next division. These assumptions yield the following, when $x < (1+\phi)g_1$:

$$A\rho_\phi(x) = \rho\left(\frac{x}{1+\phi g_1}\right);$$

when $x \geq (1+\phi)g_1$, $A\rho_\phi(x) = \rho(x - \phi g_1)$, and similarly,

$$Aw_\phi(\tau) = w\left(\frac{\tau}{1+\phi g_1}\right),$$

where $A$ indicates that these expressions must be renormalized. Thus, the cell cycle completion distribution may be propagated forward during a time step in which the drug acts using the following expression:

$$\rho_{\Delta t}(y) = A \left[ \begin{array}{l} \int_0^y w_\phi\left(\tau = \frac{\Delta t}{y-x}\right) \frac{d\tau}{dy}\rho_\phi(x)dx \\ +2\int_0^1 w\left\{\tau = \frac{\Delta t}{[(1+\phi g_1)+y]-x}\right\} \frac{d\tau}{dy}\rho_\phi(x)dx \end{array} \right].$$

### Statistical analysis

To show significance, we used a one-way nonparametric ANOVA (we did not assume Gaussian distributions given the shapes of the histograms). We performed the Kruskal–Wallis test. We also performed follow-up tests comparing the mean rank of each column with the mean rank of a control column of HEK 293A. We performed Dunn's multiple comparisons test and obtained the corresponding P value.

For comparison between two groups such as the birth volume and peak volume in Fig. 1 N, we performed an unpaired nonparametric Mann–Whitney test. For comparison between protein-expression experiments via qIF, we used a one-way ANOVA analysis with a Brown–Forsythe test.

### Online supplemental material

Fig. S1 shows supplementary information on image processing of the FX method for cell volume quantification, cell area information on the HEKs, and shRNA experiment results. Fig. S2 shows growth rate characterization under linear fitting and dye endocytosis investigation. Fig. S3 shows theoretical simulation results for cell age, cell cycle completion, and cell volume distribution, and

spherical cap fitting of cell shape of the HEKs. Fig. S4 shows supplementary information on rapamycin and cell volume, as well as pS6 and nuclear YAP/TAZ expression. Fig. S5 shows confocal imaging quantification results for pMLC of the HEKs.

## References

Aifuwa, I., A. Giri, N. Longe, S.H. Lee, S.S. An, and D. Wirtz. 2015. Senescent stromal cells induce cancer cell migration via inhibition of RhoA/ROCK/myosin-based cell contractility. *Oncotarget.* 6:30516–30531. https://doi.org/10.18632/oncotarget.5854

Bottier, C., C. Gabella, B. Vianay, L. Buscemi, I.F. Sbalzarini, J.J. Meister, and A.B. Verkhovsky. 2011. Dynamic measurement of the height and volume of migrating cells by a novel fluorescence microscopy technique. *Lab Chip.* 11:3855–3863. https://doi.org/10.1039/c1lc20807a

Burke, C.W., J.S. Suk, A.J. Kim, Y.H. Hsiang, A.L. Klibanov, J. Hanes, and R.J. Price. 2012. Markedly enhanced skeletal muscle transfection achieved by the ultrasound-targeted delivery of non-viral gene nanocarriers with microbubbles. *J. Control. Release.* 162:414–421. https://doi.org/10.1016/j.jconrel.2012.07.005

Cadart, C., E. Zlotek-Zlotkiewicz, L. Venkova, O. Thouvenin, V. Racine, M. Le Berre, S. Monnier, and M. Piel. 2017. Fluorescence eXclusion Measurement of volume in live cells. *Methods Cell Biol.* 139:103–120. https://doi.org/10.1016/bs.mcb.2016.11.009

Cadart, C., S. Monnier, J. Grilli, P.J. Sáez, N. Srivastava, R. Attia, E. Terriac, B. Baum, M. Cosentino-Lagomarsino, and M. Piel. 2018. Size control in mammalian cells involves modulation of both growth rate and cell cycle duration. *Nat. Commun.* 9:3275. https://doi.org/10.1038/s41467-018-05393-0

Chang, L., L. Azzolin, D. Di Biagio, F. Zanconato, G. Battilana, R. Lucon Xiccato, M. Aragona, S. Giulitti, T. Panciera, A. Gandin, et al. 2018. The SWI/SNF complex is a mechanoregulated inhibitor of YAP and TAZ. *Nature.* 563:265–269. https://doi.org/10.1038/s41586-018-0658-1

Conlon, I.J., G.A. Dunn, A.W. Mudge, and M.C. Raff. 2001. Extracellular control of cell size. *Nat. Cell Biol.* 3:918–921. https://doi.org/10.1038/ncb1001-918

Dannhauser, D., D. Rossi, M. Ripaldi, P.A. Netti, and F. Causa. 2017. Single-cell screening of multiple biophysical properties in leukemia diagnosis from peripheral blood by pure light scattering. *Sci. Rep.* 7:12666. https://doi.org/10.1038/s41598-017-12990-4

Dupont, S., L. Morsut, M. Aragona, E. Enzo, S. Giulitti, F. Zanconato, J. Le Digabel, M. Forcato, S. Bicciato, et al. 2011. Role of YAP/

TAZ in mechanotransduction. *Nature.* 474:179–183. https://doi.org/10.1038/nature10137

Elosegui-Artola, A., I. Andreu, A.E.M. Beedle, A. Lezamiz, M. Uroz, A.J. Kosmalska, R. Oria, J.Z. Kechagia, P. Rico-Lastres, A.L. Le Roux, et al. 2017. Force Triggers YAP Nuclear Entry by Regulating Transport across Nuclear Pores. *Cell.* 171:1397–1410.e14. https://doi.org/10.1016/j.cell.2017.10.008

Fingar, D.C., S. Salama, C. Tsou, E. Harlow, and J. Blenis. 2002. Mammalian cell size is controlled by mTOR and its downstream targets S6K1 and 4EBP1/eIF4E. *Genes Dev.* 16:1472–1487. https://doi.org/10.1101/gad.995802

Ginzberg, M.B., R. Kafri, and M. Kirschner. 2015. Cell biology. On being the right (cell) size. *Science.* 348:1245075. https://doi.org/10.1126/science.1245075

Ginzberg, M.B., N. Chang, H. D'Souza, N. Patel, R. Kafri, and M.W. Kirschner. 2018. Cell size sensing in animal cells coordinates anabolic growth rates and cell cycle progression to maintain cell size uniformity. *eLife.* 7:e26957. https://doi.org/10.7554/eLife.26957

Guo, M., A.F. Pegoraro, A. Mao, E.H. Zhou, P.R. Arany, Y. Han, D.T. Burnette, M.H. Jensen, K.E. Kasza, J.R. Moore, et al. 2017. Cell volume change through water efflux impacts cell stiffness and stem cell fate. *Proc. Natl. Acad. Sci. USA.* 114:E8618–E8627. https://doi.org/10.1073/pnas.1705179114

Horie, M., A. Saito, M. Ohshima, H.I. Suzuki, and T. Nagase. 2016. YAP and TAZ modulate cell phenotype in a subset of small cell lung cancer. *Cancer Sci.* 107:1755–1766. https://doi.org/10.1111/cas.13078

Kafri, R., J. Levy, M.B. Ginzberg, S. Oh, G. Lahav, and M.W. Kirschner. 2013. Dynamics extracted from fixed cells reveal feedback linking cell growth to cell cycle. *Nature.* 494:480–483. https://doi.org/10.1038/nature11897

Kozma, S.C., and G. Thomas. 2002. Regulation of cell size in growth, development and human disease: PI3, PKB and S6K. *BioEssays.* 24:65–71. https://doi.org/10.1002/bies.10031

Lloyd, A.C. 2013. The regulation of cell size. *Cell.* 154:1194–1205. https://doi.org/10.1016/j.cell.2013.08.053

Meng, Z., T. Moroishi, V. Mottier-Pavie, S.W. Plouffe, C.G. Hansen, A.W. Hong, H.W. Park, J.S. Mo, W. Lu, S. Lu, et al. 2015. MAP4K family kinases act in parallel to MST1/2 to activate LATS1/2 in the Hippo pathway. *Nat. Commun.* 6:8357. https://doi.org/10.1038/ncomms9357

Mir, M., Z. Wang, Z. Shen, M. Bednarz, R. Bashir, I. Golding, S.G. Prasanth, and G. Popescu. 2011. Optical measurement of cycle-dependent cell growth. *Proc. Natl. Acad. Sci. USA.* 108:13124–13129. https://doi.org/10.1073/pnas.1100506108

Perez-Gonzalez, N., J. Tao, N.D. Rochman, D. Vig, E. Chiu, D. Wirtz, and S.X. Sun. 2018. Cell tension and mechanical regulation of cell volume. *Mol. Biol. Cell.* 29:2509–2601. https://doi.org/10.1091/mbc.E18-04-0213

Petrie, R.J., and H. Koo. 2014. Direct measurement of intracellular pressure. *Curr. Protoc. Cell Biol.* 63:1–9.

Piccolo, S., S. Dupont, and M. Cordenonsi. 2014. The biology of YAP/TAZ: hippo signaling and beyond. *Physiol. Rev.* 94:1287–1312. https://doi.org/10.1152/physrev.00005.2014

Plouffe, S.W., Z. Meng, K.C. Lin, B. Lin, A.W. Hong, J.V. Chun, and K.L. Guan. 2016. Characterization of Hippo pathway components by gene inactivation. *Mol. Cell.* 64:993–1008. https://doi.org/10.1016/j.molcel.2016.10.034

Plouffe, S.W., K.C. Lin, J.L. Moore III, F.E. Tan, S. Ma, Z. Ye, Y. Qiu, B. Ren, and K.L. Guan. 2018. The Hippo pathway effector proteins YAP and TAZ have both distinct and overlapping functions in the cell. *J. Biol. Chem.* 293:11230–11240. https://doi.org/10.1074/jbc.RA118.002715

Rochman, N.D., D.M. Popescu, and S.X. Sun. 2018. Ergodicity, hidden bias and the growth rate gain. *Phys. Biol.* 15:036006. https://doi.org/10.1088/1478-3975/aab0e6

Sakaue-Sawano, A., H. Kurokawa, T. Morimura, A. Hanyu, H. Hama, H. Osawa, S. Kashiwagi, K. Fukami, T. Miyata, H. Miyoshi, et al. 2008. Visualizing spatiotemporal dynamics of multicellular cell-cycle progression. *Cell.* 132:487–498. https://doi.org/10.1016/j.cell.2007.12.033

Schmidt, E.K., G. Clavarino, M. Ceppi, and P. Pierre. 2009. SUnSET, a non-radioactive method to monitor protein synthesis. *Nat. Methods.* 6:275–277. https://doi.org/10.1038/nmeth.1314

Son, S., A. Tzur, Y. Weng, P. Jorgensen, J. Kim, M.W. Kirschner, and S.R. Manalis. 2012. Direct observation of mammalian cell growth and size regulation. *Nat. Methods.* 9:910–912. https://doi.org/10.1038/nmeth.2133

Stukalin, E.B., I. Aifuwa, J.S. Kim, D. Wirtz, and S.X. Sun. 2013. Age-dependent stochastic models for understanding population fluctuations in continuously cultured cells. *J. R. Soc. Interface.* 10:20130325. https://doi.org/10.1098/rsif.2013.0325

Sung, Y., A. Tzur, S. Oh, W. Choi, V. Li, R.R. Dasari, Z. Yaqoob, and M.W. Kirschner. 2013. Size homeostasis in adherent cells studied by synthetic phase microscopy. *Proc. Natl. Acad. Sci. USA.* 110:16687–16692. https://doi.org/10.1073/pnas.1315290110

Tao, J., and S.X. Sun. 2015. Active biochemical regulation of cell volume and a simple model of cell tension response. *Biophys. J.* 109:1541–1550. https://doi.org/10.1016/j.bpj.2015.08.025

Tumaneng, K., R.C. Russell, and K.L. Guan. 2012. Organ size control by Hippo and TOR pathways. *Curr. Biol.* 22:R368–R379. https://doi.org/10.1016/j.cub.2012.03.003

Uroz, M., S. Wistorf, X. Serra-Picamal, V. Conte, M. Sales-Pardo, P. Roca-Cusachs, R. Guimerà, and X. Trepat. 2018. Regulation of cell cycle progression by cell-cell and cell-matrix forces. *Nat. Cell Biol.* 20:646–654. https://doi.org/10.1038/s41556-018-0107-2

Varsano, G., Y. Wang, and M. Wu. 2017. Probing mammalian cell size homeostasis by channel-assisted cell reshaping. *Cell Reports.* 20:397–410. https://doi.org/10.1016/j.celrep.2017.06.057

Wang, M., N. Chai, B. Sha, M. Guo, J. Zhuang, F. Xu, and F. Li. 2018. The effect of substrate stiffness on cancer cell volume homeostasis. *J. Cell. Physiol.* 233:1414–1423. https://doi.org/10.1002/jcp.26026

Yang, Q., and K.L. Guan. 2007. Expanding mTOR signaling. *Cell Res.* 17:666–681. https://doi.org/10.1038/cr.2007.64

Zhao, B., X. Wei, W. Li, R.S. Udan, Q. Yang, J. Kim, J. Xie, T. Ikenoue, J. Yu, L. Li, et al. 2007. Inactivation of YAP oncoprotein by the Hippo pathway is involved in cell contact inhibition and tissue growth control. *Genes Dev.* 21:2747–2761. https://doi.org/10.1101/gad.1602907

Zhao, B., X. Ye, J. Yu, L. Li, W. Li, S. Li, J. Yu, J.D. Lin, C.Y. Wang, A.M. Chinnaiyan, et al. 2008. TEAD mediates YAP-dependent gene induction and growth control. *Genes Dev.* 22:1962–1971. https://doi.org/10.1101/gad.1664408

Zlotek-Zlotkiewicz, E., S. Monnier, G. Cappello, M. Le Berre, and M. Piel. 2015. Optical volume and mass measurements show that mammalian cells swell during mitosis. *J. Cell Biol.* 211:765–774. https://doi.org/10.1083/jcb.201505056